Coherence Beamforming and its Applications to the Difficult-to-Image Patient

Jeremy J. Dahl,[1] Dongwoon Hyun,[1] You Li,[1] Marko Jakovljevic,[1] Muyinatu A. L. Bell,[2]
Will J. Long,[3] Nick Bottenus,[3] Vaibhav Kakkad,[3] and Gregg E. Trahey[3]

[2]Department of Radiology, Stanford University, Stanford, CA 94305
[2]Department of Electrical and Computer Engineering, Johns Hopkins University, Baltimore, MD 21218
[3]Department of Biomedical Engineering, Duke University, Durham, NC 27708
jeremy.dahl@stanford.edu

***Abstract*—Poor quality ultrasound images and inadequate or suboptimal visualization of imaging targets is a common problem in individuals that are overweight or obese. Acoustic reverberation is an incoherent noise source that is a common factor in overweight and obese individuals and is a significant contributor to the poor image quality. Specifically, diffuse acoustic reverberation is problematic because it appears similar to common tissue texture in ultrasound images, thereby exacerbating the inadequate and suboptimal visualization.**

We describe the coherence imaging technique called the short-lag spatial coherence (SLSC) beamformer and its related imaging methods as potential solutions to the inadequate and suboptimal visualization problem. The SLSC beamformer detects the spatial similarity of the backscattered ultrasound waves, with a greater emphasis on the spatial similarity at closely-spaced positions. Because diffuse reverberation is spatially incoherent in the wavefield, noise can be differentiated from tissue and other desired imaging targets.

Applications of the SLSC beamformer to *in vivo* imaging and adaptations of the technique to other imaging modalities, including flow imaging, molecular ultrasound imaging, and photoacoustic imaging are reviewed. Although computationally more intensive than conventional delay-and-sum beamforming, we describe several techniques for fast computation of coherence, which enable real-time imaging. The challenges and criticisms of spatial coherence beamforming are reviewed, including the loss in phase information and the nonlinear behavior of the technique.

I. Introduction

Inadequate visualization of human anatomy and function with medical imaging is a rising challenge. Often, inadequate visualization is linked with overweightedness and obesity, or "body habitus" [1–7]. While the rates of overweightedness have roughly remained constant over the last several decades [8], the rates of obesity have risen dramatically [9–11]. In the United States, it is estimated that 34.2% of U.S. adults are overweight (BMI 25.0–29.9) and 35.1% are obese (BMI $\geq$30.0) [8]. Within the European Union, approximately 34.8% of the adult population were overweight and 15.4% were obese [12].

In a retrospective analysis examining the effect of obesity on image quality over all imaging modalities, Uppot et al. [1] found a very strong correlation between patient weight (or "habitus-limited") and poor image quality, with abdominal ultrasound showing the highest rate of habitus-limited studies [1]. Similarly, a study by Finkelhor et al. [13] found that 49.7% of individuals requiring outpatient echocardiography were obese, and of these individuals, obese patients had image quality ratings of poor in 14% of cases, compared to 3.9% of cases for normal weight patients.

Factors contributing to poor ultrasound image quality include the inability to obtain a good acoustic window, high attenuation of fatty or scar tissue, thickness of the subcutaneous fat layers, inhomogeneities in attenuation, variations in the speed of sound of tissue, reverberation, and off-axis scattering. Although many of these factors are present in overweight and obese patients, the can be present in normal-sized patients can as well. Patients exhibiting these characteristics are often called the "difficult-to-image patient."

Given the significant and increasing number of poor quality ultrasound exams due to difficult-to-image patients, there is a need for better ultrasonic imaging methods to combat poor image quality. Early image quality improvement methods focused on eliminating aberration of the ultrasonic wavefronts [14–16]. However, *in vivo* improvements in image quality with phase aberration correction techniques have been limited [17–19] and real-time efforts have proved difficult due to the need for multi-dimensional arrays and the lack of sufficient frame rate with phase correction algorithms [17, 19–21].

In a simulation study examining phase aberration and acoustic reverberation, two sources of noise in ultrasound imaging, Pinton et al. [22] found that image clutter due to acoustic reverberation introduced image quality degradation as strong as phase aberration. Like phase aberration, there are a few clinical practices able to mitigate the impact of acoustic reverberation. Typically, compression of the skin and fat layers with the transducer and tissue harmonic imaging are applied to obtain a good acoustic window and decrease the thickness of the fat layers, thereby minimizing reverberation between connective tissue and fat [23]. This method sometimes yields satisfactory results with overweight and obese individuals, however the force and positioning required over the course of an exam often results in ergonomic difficulties and injuries for sonographers [24]. Tissue harmonic imaging is a technique that is known to reduce acoustic clutter [25, 26]. Many studies report anecdotal evidence of harmonic imaging providing more

useful information in obese patients [27–30]. However, in the study by Pinton et al., it was shown that tissue harmonic images did not fully eliminate acoustic clutter [22].

A variety of recent approaches to reduce clutter from acoustic reverberation have been proposed, including SURF imaging [31, 32], PCA filtering [33, 34], aperture domain modeling and regularization (the ADMIRE algorithm) [35], and spatial prediction filtering [36]. In addition, techniques based on the quantification of the coherence of ultrasound backscatter were utilized to improve image quality. Initially, these "coherence factors" were proposed to describe the focusing characteristics of an imaging system with respect to phase aberration [37–39]. Li and Li [40] utilized a modified form of the coherence factor, called the generalized coherence factor (GCF), to weight B-mode images in order to reduce clutter from phase aberrations. A similar pair of coherence metrics, called the phase coherence factor (PCF) and the sign coherence factor (SCF) [41] were proposed to reduce clutter originating from beam sidelobes (which are often elevated due to aberration), and operated as a weight to the B-mode image, much like the GCF.

Clutter due to acoustic reverberation, however, imparts different coherence characteristics than phase aberration [42, 43]. The coherence characteristics of ultrasonic backscatter and acoustic reverberation can be exploited to differentiate tissue signal from noise. In the following, we review the coherence beamforming technique called the short-lag spatial coherence (SLSC) beamformer [44] and its related imaging methods as potential solutions to the inadequate and suboptimal visualization problem. We examine the techniques in their application to difficult-to-image patients and difficult-to-image scenarios. We also review the limitations and challenges of utilizing this technique.

II. Spatial Coherence

Coherence is a general term used to describe the similarity between two functions or signals. In the context here, we wish to describe the spatial similarity of a specific random process; that is, a reflected ultrasound wave that has propagated from its reflection point to the transducer and has been spatially sampled by a transducer array. Spatial coherence in this context refers to the similarity of the wave that has been sampled by the array at two different points (or elements), accounting for time-delay differences that may exist due to path-length differences. Spatial coherence of backscattered ultrasound waves can be measured or described using various metrics including covariance, correlation, and sum of absolute differences, among others [45–49]. In fact, the spatial covariance of the backscattered ultrasound wave can be described theoretically by an adapted form of the van Cittert-Zernike theorem [45].

The spatial covariance over time period T_0 between two discretely sampled ultrasound signals (i.e. channel or element signals), $s_{x_1}(n)$ and $s_{x_2}(n)$, is given by

$$C(x_1, x_2) = \int_{t-T_0/2}^{t+T_0/2} s_{x_1}(t) s_{x_2}(t)\, dt. \tag{1}$$

The ultrasound signals, $s_{x_1}(n)$ and $s_{x_2}(n)$, can be described as a wide-sense stationary random process, meaning that the spatial covariance in Eq. 1 is a function of spatial lag $\Delta x = x_2 - x_1$. In the case of transducer elements, the spatial lag can be normalized by the transducer pitch so that it is in the form of an integer number of elements, m. In the discretely sampled case, the spatial covariance at time sample n is

$$C(n, m) = \sum_{k=n-K/2}^{n+K/2} s_i(k) s_{i+m}(k). \tag{2}$$

where K is an integer number of samples that defines the kernel size over which the spatial covariance is computed.

Fig. 1 shows the normalized spatial covariance measured from several imaging targets including a point target, diffuse scatterers in a tissue-mimicking phantom, *in vivo* liver tissue, and the lumen region of *in vivo* bladder. The point target is known as a "coherent" target, because the wavefront has high spatial covariance at all lags. Because there are no echoes in the lumen of the bladder, the received signals from this target are a result of spatially "incoherent noise," meaning that the received signals or echoes have no spatial relationship. Incoherent noise sources include acoustic reverberation and noise from the ultrasound system's electronics. In the case of diffuse scatterers, the van Cittert-Zernike theorem predicts that the normalized spatial covariance from such randomly-positioned sub-wavelength scatterers imaged by a transducer array with uniform apodization is a linearly decreasing function of lag from 1 at a lag of 0 to 0 at a lag equal to N-1, where N is the number of transmitting elements in the transducer array. Although the backscatter from liver tissue is mainly a result of scattering from diffuse scatterers, Fig. 1 shows that the measured coherence deviates from the linear function predicted by the van Cittert-Zernike theorem. In this case, there is an immediate drop in the spatial covariance at the lags near 0 and a somewhat linear decrease in covariance from there. Pinton et al. [43] showed that this particular shape of the spatial covariance function is the result of the spatial coherence of incoherent noise superimposed on the spatial coherence of diffuse scatterers.

III. SLSC Beamforming

A. Formulation

The output of a delay-and-sum beamformer from the signals in Fig. 1, with the exception of the point target, is a speckle pattern. In the case of incoherent noise from electronics, which is introduced after transduction of the acoustic waves, the speckle pattern is much finer and is easier to distinguish from tissue, particularly since it changes from frame-to-frame. However, in the case of incoherent noise from acoustic reverberation, the noise is bandlimited by the bandwidth of

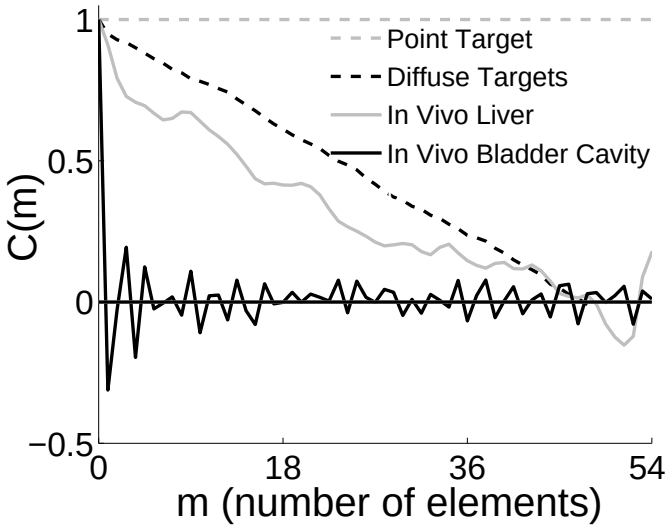

Fig. 1. The normalized spatial covariance of several imaging targets as a function of element spacing m. For a point target, the wavefront is completely coherent, while the signals from the bladder cavity echoes are completely incoherent. For diffuse scatterers, the spatial coherence decreases linearly from 1 to 0 over a length equal to the size of the transmit aperture. In the case of *in vivo* tissue, the spatial covariance deviates from the ideal diffuse scatterers due to the presence of incoherent noise. The resulting spatial covariance of tissue is a superposition of the spatial covariance of diffuse scatterers and incoherent noise.

the transducer and therefore produces a speckle pattern very similar to that of tissue [23]. The acoustic reverberation in this case can be called diffuse reverberation, in order to distinguish it from the well-known "coherent" reverberations that occurs from the specular reflections from highly-reflecting tissue boundaries (e.g. carotid wall). The diffuse reverberation can create a false impression of tissue being present where it may not exist [23], particularly because it is temporally stable. An example of acoustic noise presenting similar texture to tissue is shown in the B-mode image (top) in Fig. 2.

The short-lag spatial coherence (SLSC) beamformer exploits the differences in the spatial coherence to create images that suppress diffuse reverberation clutter and electronic noise. In Fig. 1, the difference in spatial coherence between pure acoustic noise and tissue is relatively small at the larger lags. However, in the region of shorter lags (e.g. 1–18), there are large differences between the received waveforms from tissue and noise. The SLSC beamformer therefore utilizes the "short-lag" region as its basis to differentiate tissue signal from noise.

In traditional SLSC beamforming, spatial coherence is measured by a normalized cross-correlation function, typically in the form [44]:

$$\hat{R}(n,m) = \frac{1}{N-m} \sum_{i=1}^{N-m} \frac{\sum_{k=n-K/2}^{n+K/2} s_i(k) s_{i+m}(k)}{\sqrt{\sum_{k=n-K/2}^{n+K/2} s_i^2(k) \sum_{k=n-K/2}^{n+K/2} s_{i+m}^2(k)}} \tag{3}$$

The normalized cross-correlation function is then integrated or summed over the lower-lag region to produce the image at sample n:

$$SLSC(n) = \sum_{m=1}^{M} \hat{R}(n,m), \tag{4}$$

where M indicates the maximum lag to integrate or sum over and $M < N$. Typically, M is a value in the range corresponding to 5–30% of the transmit aperture width (i.e. the so-called "short-lag region"). The selection of M varies depending on the imaging scenario, with simulated and phan-

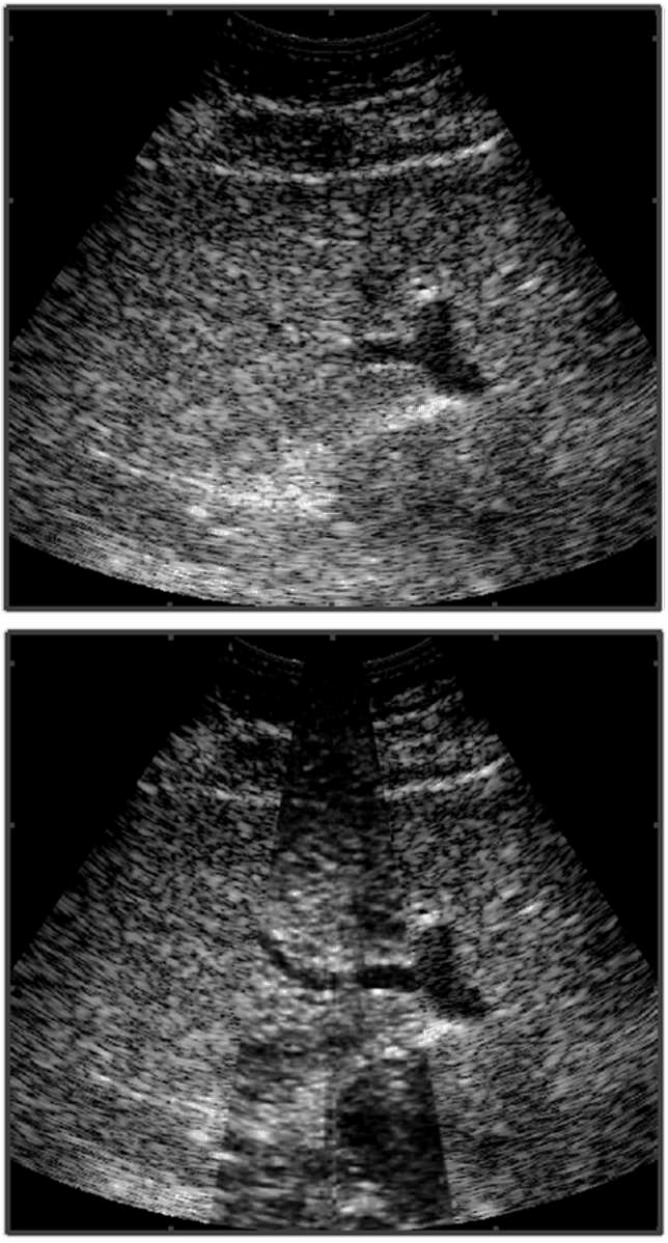

Fig. 2. (top) B-mode image of the liver. Acoustic reverberation is present in this image, but is difficult to detect because it appears similar to tissue texture. (bottom) An SLSC images of the same liver, demonstrating a suppression of the noise and an improvement in the visibility of anatomical structures that are otherwise not visible due to the acoustic noise.

tom images typically using the higher end of this range and *in vivo* images typically using the lower end of this range. In addition, while the exact spatial coherence computation can be varied, the normalization aspect of it is important, because large amplitude noise can dominate the image, even if only small amount of coherence are present. An example of an SLSC image and its impact on the suppression of acoustic noise is shown in the bottom image of Fig. 2.

B. Image Characteristics

SLSC images look similar to B-mode images, but there are several key differences. Because of the normalized signals, the dynamic range of SLSC images is much smaller than that of B-mode images and are better displayed using linear scales rather than compressed scales, although in cases of relatively high noise, light compression of the SLSC image can be utilized to improve image quality [50]. In some cases, the SLSC image can many times yield negative values, because the normalized spatial coherence function can take on negative values. Regardless, visual contrast of SLSC images is often improved by utilizing a normalized display range of [0,1].

In addition, The contrast mechanism in SLSC images is wavefront coherence, with bright pixels indicating high coherence and dark pixels indicate little or no coherence. Thus, in images that have regions of high-amplitude noise, the SLSC image will be dark while the B-mode image generally shows speckle or a hazy appearance. Compared to B-mode images, the contrast mechanism of SLSC makes for useful anatomical imaging but not for quantitative comparisons related to echo amplitude. SLSC images are specifically designed for noisy imaging conditions, and therefore do not necessarily produce better images than B-mode when the SNR is high, but rather show much more dramatic improvements in image quality when the SNR is low [50].

Ideally, SLSC images should show a constant value with diffuse scatterers, but the statistical variation of these imaging targets yield a texture similar to, but smoother than, speckle. In general, the speckle signal-to-noise ratio (μ/σ) is far higher in SLSC imaging than in B-mode, and contrast targets such as lesions generally have greater contrast and contrast-to-noise ratio (CNR) in SLSC imaging than in B-mode [44, 50].

A less intuitive characteristic of SLSC images is the source of contrast between two adjacent regions of diffuse scatterers with different echo amplitudes. In this case, one would assume that, due to the normalization in the SLSC computation, there should be no contrast between these two regions because they should produce the same spatial coherence function. However, sidelobes from the transmit beam generate off-axis echoes from the higher-amplitude region, which interfere with the echoes in the lower-amplitude region. These off-axis echoes introduce incoherent noise in the echoes from the low-amplitude region, thereby decreasing the SLSC value and generating contrast. As the distance into the lower amplitude region grows, the off-axis signals become weaker and have less an impact on the SLSC value. At sufficiently large distances, the image value in the lower-amplitude region is the same as the higher-amplitude region [44]. This effect is more apparent in simulated and phantom images with low noise, but is not often seen *in vivo* where acoustic and thermal noise is almost always present and often hide this effect. Indeed, if incoherent noise is added to the element signals in simulations and phantoms, the effect is not observed [44, 50, 51]. Similarly, randomization of the apodization of transmit aperture acts like noise and can yield the same effect [52].

Resolution in SLSC images is dependent on several factors [51]. Axial resolution is affected by the kernel size, K, and is therefore slightly less than B-mode images, although methods to achieve equivalent axial resolution to B-mode imaging is described in the following section. Lateral resolution is more difficult to quantify because it depends on the short-lag cutoff, M, as well as the SNR of the element signals. Generally, a smaller M corresponds to poorer resolution, as does a higher SNR. Larger M and lower SNR correspond to higher lateral resolution. In practice, the parameters and imaging conditions selected for SLSC images generally lead to slightly worse lateral resolution than B-mode imaging.

The depth-of-field (DOF) of SLSC images is dependent on the transmitted pressure field. Narrow transmit beams generate high- or partially-coherent wavefronts, while broad transmit beams generate low-coherence wavefronts. In conventional transmission with a fixed focus transmit beam, the DOF of the resulting SLSC images is limited and often produces images that are dark at the shallower depths, prior to the transmit focal depth. Plane wave and broad transmissions are not well suited for SLSC imaging, unless the transmissions are used to generate synthetic transmit focusing [53], in which case a narrow transmit beam is achieved at all locations thereby producing high quality SLSC images.

C. Efficient SLSC Beamforming

The formulation of Eq. 3 is computationally demanding, requiring orders of magnitude larger computational times than traditional delay-and-sum beamforming. In addition, a finite kernel size, K, is necessary in Eq. 3 in order to appropriately normalize the coherence function. While the finite kernel size improves texture SNR, it reduces resolution and increases computational effort [54].

Application of SLSC beamforming in medical ultrasound therefore requires faster and more efficient means. Hyun et al. [54] proposed a series of computationally efficient approaches to SLSC beamforming including computation of SLSC using K=1 by use of a complex cross-correlation, downsampling or subaperture beamforming in the aperture dimension, and utilization of an ensemble calculation of Eq. 3.

Assuming $s_i(n)$ is quasi-monochromatic, we can express the channel signal in terms of a complex phasor $s_i(n) = \Re\{\mathbf{S}_i(n)e^{j\mathbf{\Phi}_i(n)}\}$, where $\mathbf{S}_x$ and $\mathbf{\Phi}_x$ are the magnitude and phase of the channel signal. The covariance between two complex signals $\mathbf{s}_i(n)$ and $\mathbf{s}_{i+m}(n)$ is then

$$\begin{aligned}\mathbf{C}(n) &= E\{\mathbf{s}_i(n)\mathbf{s}^*_{i+m}(n)\} \\ &= E\left\{\mathbf{S}_i(n)\mathbf{S}_{i+m}(n)e^{j\left(\mathbf{\Phi}_i(n)-\mathbf{\Phi}_{i+m}(n)\right)}\right\}, \quad (5)\end{aligned}$$

where * indicates the complex conjugate. For a real-valued signal expressed as a complex-valued signal, the covariance of the real-valued signal, $C(n,m)$, is equal to half the real part of the complex covariance $\mathbf{C}(n,m)$ [55], or

$$\begin{aligned} C(n,m) &= \frac{1}{2}\Re\{\mathbf{C}(m)\} \\ &= E\left\{\frac{1}{2}\Re\left\{\mathbf{S}_i(n)\mathbf{S}_{i+m}(n)e^{j\left(\mathbf{\Phi}_i(n)-\mathbf{\Phi}_{i+m}(n)\right)}\right\}\right\}. \end{aligned} \tag{6}$$

If $\mathbf{s}_i(n)$ and $\mathbf{s}_{i+m}(n)$ are windowed over K samples, and the complex magnitudes $\mathbf{S}_i(n)$ and $\mathbf{S}_{i+m}(n)$ are approximately constant over the K samples, then Eq. 6 can be written as

$$C(n,m) \approx \frac{1}{2}S_iS_{i+m}\,E\left\{\Re\left\{e^{j\left(\mathbf{\Phi}_i(n)-\mathbf{\Phi}_{i+m}(n)\right)}\right\}\right\}, \tag{7}$$

where S_i and S_{i+m} are constants. Using Eq. 7, the normalized cross-correlation between $\mathbf{s}_i(n)$ and $\mathbf{s}_{i+m}(n)$ reduces to

$$\begin{aligned} \hat{R}(n,m) &\approx E\left\{\cos\left(\mathbf{\Phi}_i(n)-\mathbf{\Phi}_{i+m}(n)\right)\right\} \\ &\approx \frac{1}{K}\sum_{k=1}^{K}\cos\left(\phi_i(n)-\phi_{i+m}(n)\right), \end{aligned} \tag{8}$$

where $\phi_i(n)$ and $\phi_{i+m}(n)$ are the phases of signals at sample n. Eq. 8 is the estimated normalized cross-correlation between the two element signals computed over a kernel length K, and can approximate the normalized cross-correlation when K=1. Eq. 8 is equivalent to taking the norm of the complex multiplication $\mathbf{s}_i(n)\mathbf{s}^*_{i+m}(n)$ [54], or

$$\hat{R}(n,m) = \frac{\mathbf{s}_i(n)\mathbf{s}^*_{i+m}(n)}{|\mathbf{s}_i(n)|\left|\mathbf{s}^*_{i+m}(n)\right|}. \tag{9}$$

Using the formulation described in Eq. 9, Hyun et al. [54] showed that spatial coherence computation time could improved by a factor of 6.2 compared to conventional computation using a kernel equal to a wavelength. In addition, axial resolution of the SLSC images improves, but at the expense of a loss in texture SNR.

Computational efficiency is also attained by taking advantage of the redundancy of spatial coherence information across the aperture. This form of efficiency can be realized either through subaperture delay-and-sum beamforming followed by normalized cross-correlation of the beamformed subapertures [54, 56], or by utilizing a subset of the individual element signals (e.g. utilizing every P^{th} element signal) [54]. Subaperture beamforming improves computational throughput, roughly 11 times faster than traditional SLSC for subaperture sizes of 4 elements, but tends to increase overall SLSC image values and saturate the image. In comparison, uniform "downsampling" of the aperture maintains consistent SLSC image quality and achieves even greater computational throughput for the same size data; for example, a 13 times faster throughput than traditional SLSC by utilizing only every fourth element signal.

While Eq. 3 describes an intuitive measurement of coherence, an "ensemble" form of Eq. 3 is shown to reduce coherence estimator variance and improve overall SLSC image quality [54]:

$$\hat{R}^{\text{ens}}_{\Delta}(m) = \frac{\sum_{\Delta} ss_m}{\sqrt{\sum_{\Delta}|s|^2\sum_{\Delta}|s_m|^2}}, \tag{10}$$

where the signals s refers to all of the channel signals over all K samples and s_m refers to the same channel signals shifted by a lag of m channels. The notation Δ is utilized to indicate the domain of all K samples over all channels.

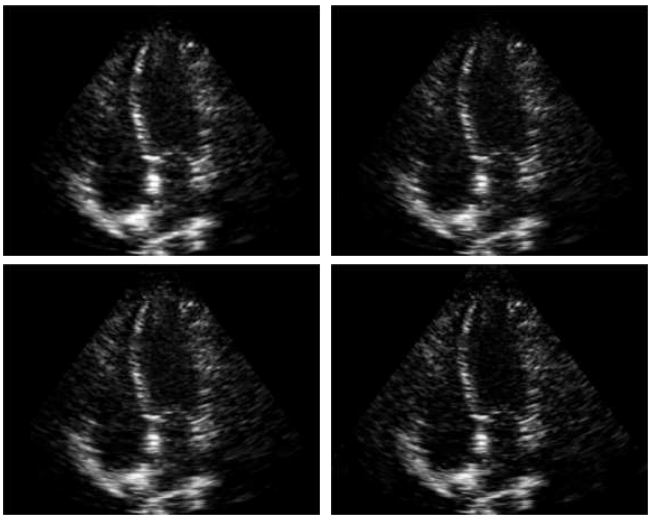

Fig. 3. (top left) Traditional SLSC image of an apical 4-chamber view of the heart using a kernel size of one wavelength. (top right) An SLSC image using the complex correlation coefficient with K=1. (bottom left) An SLSC image using the the ensemble complex correlation with K=1. (bottom right) The same SLSC image using the ensemble complex correlation with K=1 and uniform downsampling of the elements by a factor of 2.

Using an ensemble approach to coherence estimation yields a slight improvement in computational throughput. However, when combined with the complex correlation, the ensemble estimator can be used to achieve greater efficiency in SLSC image computation. In this case, an entire SLSC image can be computed by complex correlation of all of the element signals at once, with K=1, and then lowpass filtering the resulting correlations with a rectangular window of length D to achieve an effective kernel size $K = D$.

Fig. 3 shows examples of these efficient computational techniques. In the upper left is a traditional SLSC image of an apical 4-chamber view of the heart. Here, a kernel size equal to a wavelength is used to form the image using Eqs.3 and 4. In the upper right image, the complex correlation in Eq. 9 is used with K=1. The lower left image utilizes the complex correlation with the ensemble estimator in Eq. 10. The lower right image is formed using the same process as the image in the lower left, except that every other element signal is dropped from the computation. The image in the lower right has similar image quality to the image in the upper left, but can be computed 20 times faster [54].

Another highly efficient approach to SLSC imaging is to take advantage of the principle of acoustic reciprocity

[57]. Acoustic reciprocity enables the transmit and receive aperture to be exchanged in the image formation process. When combined with synthetic transmit aperture, the spatial coherence function can be computed in the transmit aperture domain, rather than in the receive aperture domain as is done conventionally. In the acoustic reciprocity approach, a single element is used for transmission, and delay-and-sum beamforming is performed to produce a "low-resolution" radiofrequency (RF) image. Instead of combining subsequent element transmissions into a "high-resolution" RF image as would be done with synthetic transmit focusing, the RF image lines are correlated between transmit events. By utilizing the downsampling of the aperture described above, high-quality and efficient SLSC images can be produced [57]. Similarly, modification of the acoustic reciprocity principle to the angular domain allows spatial coherence images to be produced for plane wave coherent compounding (i.e. plane wave synthetic transmit focusing) [58].

IV. Applications

SLSC has been applied to many imaging targets, including abdominal, cardiac, and fetal ultrasound, and particularly in respect to difficult-to-image patients. In addition, because SLSC acts as a replacement for the delay-and-sum beamformer, the beamformer can be combined with many existing ultrasonic imaging techniques, such as tissue harmonic imaging, flow imaging, contrast-enhanced ultrasound, and photoacoustic imaging. In the following, we review applications of SLSC beamforming to *in vivo* imaging and other ultrasound imaging modalities.

A. Anatomical Imaging

1) Abdominal: SLSC imaging has been applied to imaging *in vivo* liver and its vasculature [59, 60] as well as kidney [61]. In a pilot study of 17 subjects with poor, medium, and high image quality, Jakovljevic et al. [59] utilized fundamental and harmonic SLSC imaging to improve the visualization of liver tissue and its vasculature. In this study, SLSC was shown to improve contrast and CNR of the liver vascular under all imaging conditions. Greater improvement in image quality was observed with the subjects that were deemed to have poor image quality. Smaller improvements were seen in the medium and high quality images, although these results are not unexpected given that high quality images will involve less incoherent noise. In the harmonic version of SLSC imaging, significant improvements were also observed in the poor quality images, although the improvements were smaller than that of the fundamental SLSC images owing to the fact that harmonic imaging also contributes to the reduction in acoustic clutter.

2) Cardiac: Echocardiography is a promising application for SLSC imaging due to its susceptibility to many of the factors that contribute to poor image quality. Echocardiography has a limited acoustic window, meaning that there are few positions on the chest wall for which images can be obtained. If significant clutter is present in these acoustic windows, there are few opportunities to obtain images from other regions of the chest. In addition, due to the rib cage, only the tissue anterior to the rib cage can be compressed.

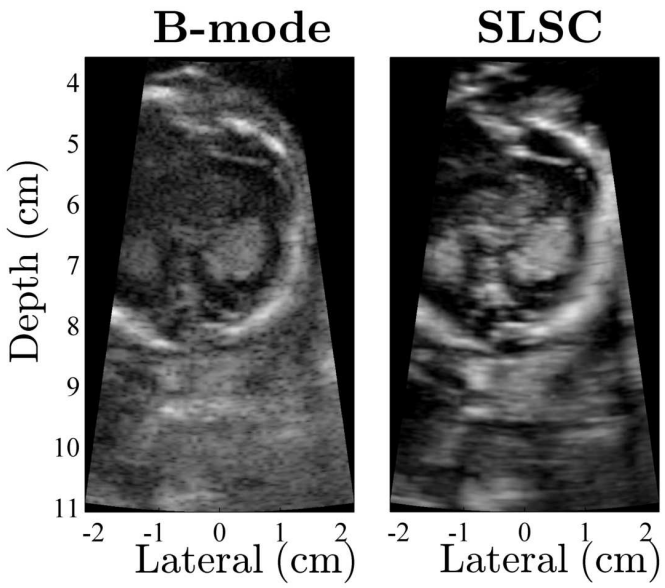

Fig. 4. SLSC images of the cerebral ventricles and brain of a fetus in a high body-mass-index (BMI$\geq$25) mother. The SLSC image shows reduced image clutter and better overall delineation of the target structure compared to the B-mode image.

In a study involving 14 patients with sonographer-identified poor image quality, SLSC imaging was compared to B-mode imaging in conventional echocardiography [62]. In this study, SLSC imaging demonstrated average contrast improvement of 8 dB and CNR improvement of 0.7. In addition, observer studies showed that SLSC decreased the number of endocardial border segments that were not observed using conventional B-mode imaging from 33% to 22%.

Hyun et al. [63] compared real-time SLSC imaging to conventional B-mode imaging in stress echocardiography patients. In this study, 15 patients were identified as having poor quality due to the inability to visualize two consecutive endocardial segments and thus required the administration of contrast agent. In this study, SLSC imaging demonstrated improvement in visualization of approximately 17% of the endocardial segments in the apical four chamber and parasternal long axis views. In one of the 15 patients, image quality was improved with SLSC imaging such that no two consecutive segments were not visualized, meaning that this patient would not have required contrast agent with SLSC imaging.

3) Fetal: Kakkad et al. [64] utilized SLSC imaging to image the fetus in pregnant women during the first trimester. In this study, 11 maternal-fetal-medicine patients were imaged and common fetal structures during the nuchal translucency (NT) exam were targeted, including bladder, stomach, cerebral ventricles, and NT. Fundamental and harmonic SLSC imaging yielded consistent texture SNR and CNR improvement over all sonographer-assessed image quality categories (good, medium, and poor). Contrast was shown to generate the largest

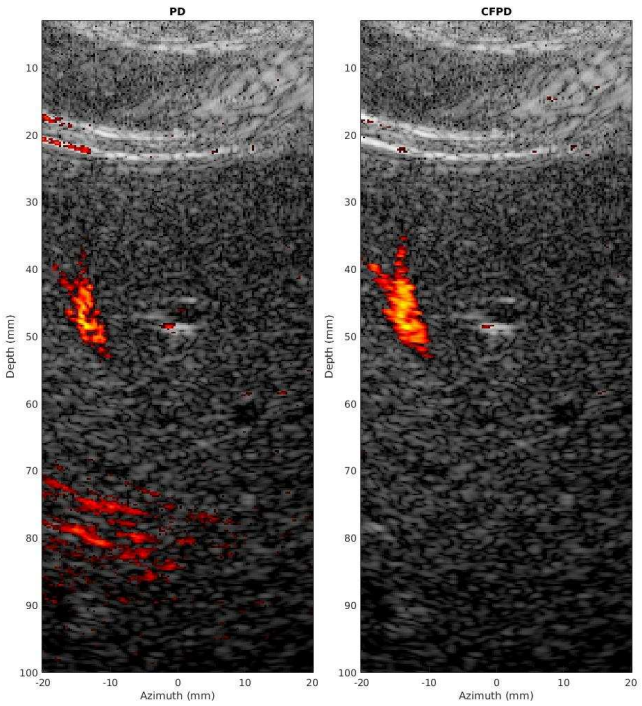

Fig. 5. A comparison of conventional power Doppler (PD) and coherent flow power Doppler (CFPD) applied to imaging of the liver vasculature. Notably, CFPD demonstrates greater SNR and suppresses artifacts in the image. Narrow branches of the demonstrated blood vessel are also better visualized in the CFPD image.

improvement in the poor quality images, with medium and high quality images showing non-significant improvement of the targeted structures. Fig. 4 shows an example comparison of B-mode and SLSC imaging of the fetal cerebral ventricles in a difficult-to-image pregnant women.

B. Flow Imaging

The sensitivity of power Doppler imaging, particularly in slow flow conditions, is limited by attenuation of the desired signal by the wall filter and noise sources including electronic noise, stationary or slowly moving tissue clutter, reverberation clutter, and off-axis scattering from tissue. Because blood signal is similar to tissue signal, albeit at a much lower amplitude, SLSC beamforming can be utilized to improve the sensitivity of power Doppler imaging. This modality, called coherent flow power Doppler, or CFPD, is shown to improve SNR of the power Doppler signal and suppress both background thermal noise and reverberation noise from tissue that leaks through the wall filter [65, 66]. This additional sensitivity can be used to improve the frame rate of power Doppler imaging, reduce flash artifact, and detect slower flow [65] using identical pulse sequences to conventional power Doppler. In small-diameter vessels CFPD is shown to increase vessel SNR by 7.5–12.5 dB under the same physiological conditions. An example of CFPD applied to imaging of liver vasculature is shown in Fig. 5.

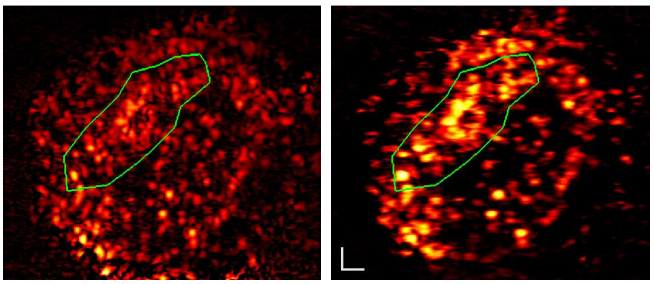

Fig. 6. SLSC beamforming applied to molecular imaging of pancreatic cancer in a mouse model. (left) Molecular ultrasound imaging utilizing delay-and-sum beamforming in the detection of pancreatic cancer. (right) Molecular ultrasound utilizing SLSC beamforming in the same tumor.

C. Molecular Ultrasound imaging

High sensitivity is critical to molecular ultrasound imaging, especially as this method transitions into clinic practice. Clinical imaging includes additional challenges that are often not observed in preclinical studies. For example, preclinical tumors in mice are usually easily accessible with high-frequency ultrasound and make wonderful images of the targeted contrast agent. However, clinical tumors are usually embedded beneath several centimeters of tissue, and include image degradation via the mechanisms of phase aberration and reverberation clutter previously described. In addition, clinical imaging frequencies are also lower than that used in small animal imaging, resulting in lower resolution. These challenges are compounded by the inherently low signal-to-noise ratio (SNR) resulting from the specialized pulses that are used to keep the microbubbles intact, as well as the need to detect low concentration of microbubbles that may be present in early stage cancers. Application of SLSC imaging to molecular ultrasound is shown in Fig. 6. In this image, the SNR of the molecular imaging signal in a transgenic mouse model of a pancreatic ductal carcinoma was improved by 9.3 dB in the outlined region (compared to molecular imaging signal in a normal tissue region outside the tumor).

D. Photoacoustic Imaging

1) Guided Surgeries: SLSC beamforming has be introduced in photoacoustic imaging to guide surgeries [67]. In endonasal surgery applications, bone impedes the optical transmission, and therefore the laser fluence is decreased, resulting in low SNR photoacoustic signals. In addition, bone is highly reflective of acoustic signals, and therefore creates incoherent reverberation within the nasal cavity. Application of photoacoustic SLSC to guide endonasal surgery was used to reduce image artifacts from the low SNR and acoustic reverberations in the nasal cavity and improve detection of blood vessels in the nasal cavity [68].

2) Brachytherapy Seed Detection: SLSC imaging is well suited to the detection of brachytherapy seeds in prostate cancer therapy. Brachytherapy seeds are difficult to detect with conventional ultrasound imaging because the seed's size, shape, and orientation influence the response of the reflected

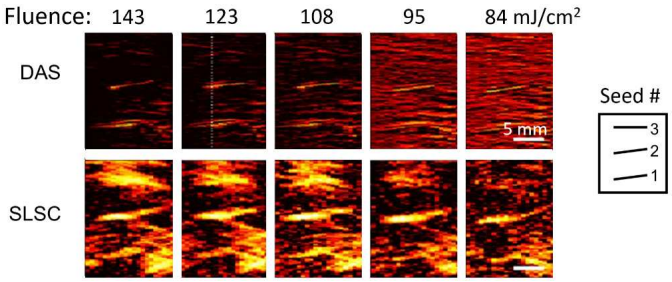

Fig. 7. Photoacoustic SLSC images of three brachytherapy seeds implanted in an *in vivo* canine prostate. It is difficult to detect all three seeds in the conventional photoacoustic images made from delay-and-sum (DAS) beamforming. SLSC beamforming better visualizes the three seeds at both lower and higher energy fluence levels [69].

wave. Photoacoustic imaging can yield better detection that conventional ultrasound because the photoacoustic effect is less impacted by the seed's size, shape, and orientation.

Bell et al. [70] showed that SLSC imaging adapted to photoacoustics for the purpose of brachytherapy seed detection can improve brachytherapy seed contrast by up to 25 dB in cases [70]. In a preclinical study of *in vivo* canine prostates, photoacoustic SLSC imaging was shown to improve brachytherapy seed contrast by up to 20 dB [69]. More recently, Bell et al. [71] developed a transurethral photoacoustic imaging system that utilizes photoacoustic SLSC imaging. In canine prostates, this system showed that photoacoustic SLSC provided uniform contrast of brachytherapy seeds with depth, while DAS-based photoacoustic imaging showed decreasing contrast of brachytherapy seeds with depth.

V. Challenges

SLSC beamforming is a technique designed to reduce the impact of incoherent noise on image quality. While the images produced with SLSC beamforming look similar to those produced with delay-and-sum beamforming, there are several aspects to this beamformer that make it inappropriate for use in some areas of ultrasound imaging.

The SLSC beamformer reduces incoherent noise in the output image, but not in the RF channel signals. The SLSC beamforming process removes the phase from the received signals, thereby making SLSC beamforming impossible for tasks that require RF signals, such as displacement or speckle tracking and velocity estimation.

One criticism of SLSC beamforming is the nonlinear response of the imaging system to echo magnitude or power. The nonlinear response occurs because the SLSC beamformer normalizes the spatial coherence function, thereby removing echo magnitude or power from the beamforming process. While delay-and-sum beamfoming produces an image response that is linear with respect to signal magnitude and flat with respect to SNR, images using SLSC beamforming produces a response that flat with respect to signal magnitude, flat at high SNR, and linear at low SNR values [51, 65]. While this type of response can be useful for anatomical imaging or detection tasks (e.g. power Doppler or molecular signal detection), it is compromised for tasks that require quantification, such as backscatter coefficient estimation or perfusion imaging.

A common artifact in SLSC images is dark regions appearing adjacent to high-magnitude signals, such as point targets. These regions occur for the same reason described in Section III-B; that is, the high-magnitude target creates strong off-axis scattering in the regions adjacent to the target, which significantly decrease the coherence of the signals in this region and thereby produce dark pixels in the SLSC image.

A significant challenge for SLSC beamforming is that it is not easily implemented on many of the existing clinical platforms. Because clinical platforms are designed to rapidly process channel signals with the delay-and-sum beamformer, proper access to the required channel signals is not easily obtained to perform SLSC beamforming. It is likely that software beamformers will be needed for wider adoption of this beamforming technique. In addition, the texture difference in SLSC images require modification to existing post-processing techniques that attempt to improve general image quality (e.g. speckle reduction). Investment in the refinement of post-processing techniques will also be required for clinical translation of this beamformer.

VI. Conclusions

Short-lag spatial coherence (SLSC) beamforming is a technique that utilizes the spatial similarity of the wavefronts sampled by the transducer aperture to form images. The beamformer is designed to mitigate image quality degradation due to incoherent noise, such as acoustic reverberation from tissue layers or noise from the ultrasound system electronics. SLSC beamforming has been adapted to many existing imaging modalities to improve image quality or provide better detection of specific targets, and has been applied to many clinical imaging scenarios. In general, SLSC images generate improved contrast, contrast-to-noise ration, and image texture compared to conventional B-mode images. While considerable improvement has been shown in cardiac, fetal, and abdominal imaging scenarios, software beamforming systems will be necessary to fully adopt this technique in the future.

Acknowledgments

Much of this work is has been supported by the National Institute of Biomedical Imaging and Bioengineering with grants R01-EB013361, R01-EB015506, R00-EB018994, and R01-EB017711 and by the Human Placenta Project through the Eunice Kennedy Shriver National Institute of Child Health and Human Development under award R01-HD086252. The authors would also like to thank Siemens Healthineers for their in-kind and technical support.

References

[1] R. N. Uppot, D. V. Sahani, P. F. Hahn, M. K. Kalra, S. S. Saini, and P. R. Mueller, "Effect of obesity on image quality: fifteen-year longitudinal study for evaluation of dictated radiology reports," *Radiology*, vol. 240, no. 2, pp. 435–439, 2006.

[2] R. N. Uppot, "Impact of obesity on radiology," *Radiologic Clinics of North America*, vol. 45, no. 2, pp. 231–246, 2007.

[3] A. Shmulewitz, S. A. Teefey, and B. S. Robinson, "Factors affecting image quality and diagnostic efficacy in abdominal sonography: A prospective study of 140 patients," *J Clin Ultrasound*, vol. 21, no. 9, pp. 623–630, 1993.

[4] H. M. Wolfe, R. J. Sokol, S. M. Martier, and I. E. Zador, "Maternal obesity: A potential source of error in sonographic prenatal diagnosis," *Obstet Gynecol*, vol. 76, no. 3 Pt 1, pp. 339–342, 1990.

[5] I. Hendler, S. C. Blackwell, E. Bujold, M. C. Treadwell, H. M. Wolfe, R. J. Sokol, and Y. Sorokin, "The impact of maternal obesity on midtrimester sonographic visualization of fetal cardiac and craniospinal structures," *Int J Obes Relat Metab Disord*, vol. 28, no. 12, pp. 1607–1611, 2004.

[6] J. V. Garrett, M. A. Passman, R. J. Guzman, J. B. Dattilo, and T. C. Naslund, "Expanding options for bedside placement of inferior vena cava filters with intravascular ultrasound when transabdominal duplex ultrasound imaging is inadequate," *Ann Vasc Surg*, vol. 18, no. 3, pp. 329–334, 2004.

[7] F. R. Khoury, H. M. Ehrenberg, and B. M. Mercer, "The impact of maternal obesity on satisfactory detailed anatomic ultrasound image acquisition," *J Matern Fetal Neonatal Med*, vol. 22, no. 4, pp. 337–341, 2009.

[8] C. L. Ogden, M. D. Carroll, B. K. Kit, and K. M. Flegal, "Prevalence of childhood and adult obesity in the United States, 2011–2012," *JAMA*, vol. 311, no. 8, pp. 806–814, 2014.

[9] K. M. Flegal, M. D. Carroll, R. J. Kuczmarski, and C. L. Johnson, "Overweight and obesity in the United States: Prevalence and trends, 1960–1994," *Int J Obes Relat Metab Disord*, vol. 22, no. 1, pp. 39–47, 1998.

[10] K. M. Flegal, M. D. Carroll, C. L. Ogden, and C. L. Johnson, "Prevalence and trends in obesity among U.S. adults, 1999–2000," *JAMA*, vol. 288, no. 14, pp. 1723–1727, 2002.

[11] K. M. Flegal, M. D. Carroll, C. L. Ogden, and L. R. Curtin, "Prevalence and trends in obesity among US adults, 1999–2008," *JAMA*, vol. 303, no. 3, pp. 235–241, 2010.

[12] E. H. I. Survey, "Overweight and obesity - bmi statistics," Retrieved from http://ec.europa.eu/eurostat/statistics-explained/index.php/Overweight_and_obesity_-_BMI_statistics and http://appsso.eurostat.ec.europa.eu/nui/show.do?dataset=hlth_ehis_bm1e&lang=en, 2014.

[13] R. S. Finkelhor, M. Moallem, and R. C. Bahler, "Characteristics and impact of obesity on the outpatient echocardiography laboratory," *Am J Cardiol*, vol. 97, no. 7, pp. 1082–1084, 2006.

[14] S. W. Flax and M. O'Donnell, "Phase-aberration correction using signals from point reflectors and diffuse scatterers: Basic principles," *IEEE Trans Ultrason Ferroelect Freq Contr*, vol. 35, no. 6, pp. 758–767, 1988.

[15] L. Nock, G. E. Trahey, and S. W. Smith, "Phase aberration correction in medical ultrasound using speckle brightness as a quality factor," *J Acoust Soc Am*, vol. 85, no. 5, pp. 1819–1833, 1989.

[16] D.-L. Liu and R. C. Waag, "Time-shift compensation of ultrasonic pulse focus degradation using least-mean-square error estimates of arrival time," *J Acoust Soc Am*, vol. 95, no. 1, pp. 542–555, 1994.

[17] K. W. Rigby, E. A. Andarawis, C. L. Chalek, B. H. Haider, , M. O'Donnell, L. S. Smith, and D. G. Wildes, "Improved *In Vivo* abdominal image quality using real-time estimation and correction of wavefront arrival time errors," in *Proc IEEE Ultrason Symp*, vol. 2, 2000, pp. 1645–1653.

[18] J. J. Dahl, M. S. Soo, and G. E. Trahey, "Clinical evaluation of combined spatial compounding and adaptive imaging in breast tissue," *Ultrason Imaging*, vol. 26, no. 4, pp. 203–216, 2004.

[19] J. J. Dahl, S. A. McAleavey, G. F. Pinton, M. S. Soo, and G. E. Trahey, "Adaptive imaging on a diagnostic ultrasound scanner at quasi real-time rates," *IEEE Trans Ultrason Ferroelect Freq Contr*, vol. 53, no. 10, pp. 1832–1843, 2006.

[20] A. T. Fernandez, K. L. Gammelmark, J. J. Dahl, C. G. Keen, R. C. Gauss, and G. E. Trahey, "Synthetic elevation beamforming and image acquisition capabilities of an 8x128 1.75D array," *IEEE Trans Ultrason Ferroelect Freq Contr*, vol. 50, no. 1, pp. 40–57, 2003.

[21] J. C. Lacefield and R. C. Waag, "Time-shift estimation and focusing through distributed aberration using multirow arrays," *IEEE Trans Ultrason Ferroelect Freq Contr*, vol. 48, no. 6, pp. 1606–1624, 2001.

[22] G. F. Pinton, G. E. Trahey, and J. J. Dahl, "Sources of image degradation in fundamental and harmonic ultrasound imaging: A nonlinear fullwave simulation study," *IEEE Trans Ultrason Ferroelect Freq Contr*, vol. 58, no. 6, pp. 1272–1283, 2011.

[23] J. J. Dahl and N. M. Sheth, "Reverberation clutter from subcutaneous tissue layers: Simulation and in vivo demonstrations," *Ultrasound Med Biol*, vol. 40, no. 4, pp. 714–726, 2014.

[24] M. Muir, P. Hrynkow, R. Chase, D. Boyce, and D. McLean, "The nature, cause, and extent of occupational musculoskeletal injuries among sonographers: Recommendations for treatment and prevention," *J Diagn Med Sonog*, vol. 20, no. 5, pp. 317–325, 2004.

[25] T. Christopher, "Finite amplitude distortion-based inhomogeneous pulse echo ultrasonic imaging," *IEEE Trans Ultrason Ferroelect Freq Contr*, vol. 44, no. 1, pp. 125–139, 1997.

[26] M. A. Averkiou, D. N. Roundhill, and J. E. Powers, "A new imaging technique based on the nonlinear properties of tissues," in *Proc IEEE Ultrason Symp*, vol. 2, 1997, pp. 1561–1566.

[27] F. Tranquart, N. Grenier, V. Eder, and L. Pourcelot, "Clinical use of ultrasound tissue harmonic imaging," *Ultrasound Med Biol*, vol. 25, no. 6, pp. 889–894, 1999.

[28] S. Choudhry, B. Gorman, J. W. Charboneau, D. J. Tradup, R. J. Beck, J. M. Kofler, and D. S. Groth, "Comparison of tissue harmonic imaging with conventional US in abdominal disease," *RadioGraphics*, vol. 20, no. 4, pp. 1127–1135, 2000.

[29] S. J. Rosenthal, P. H. Jones, and L. H. Wetzel, "Phase inversion tissue harmonic sonographic imaging: A clinical utility study," *Am J Roentgenol*, vol. 176, no. 6, pp. 1393–1398, 2001.

[30] K. S. Sodhi, R. Sidhu, M. Gulati, A. Saxena, S. Suri, and Y. Chawla, "Role of tissue harmonic imaging in focal hepatic lesions: Comparison with conventional sonography," *J Gastroenterol Hepatol*, vol. 20, no. 10, pp. 1488–1493, 2005.

[31] S. P. Näsholm, R. Hansen, S.-E. Måsøy, T. F. Johansen, and B. A. J. Angelsen, "Transmit beams adapted to reverberation noise suppression using dual-frequency SURF imaging," *IEEE Trans Ultrason Ferroelect Freq Contr*, vol. 56, no. 10, pp. 2124–2133, 2009.

[32] J. M. Rau, S.-E. Måsøy, R. Hansen, B. A. Angelsen, and T. A. Tangen, "Methods for reverberation suppression utilizing dual freqeuncy band imaging," *J Acoust Soc Am*, vol. 134, no. 3, pp. 2313–2325, 2013.

[33] M. Lediju, M. J. Pihl, S. J. Hsu, J. J. Dahl, C. M. Gallippi, and G. E. Trahey, "A motion-based approach to abdominal clutter rejection," *IEEE Trans Ultrason Ferroelect Freq Contr*, vol. 56, no. 11, pp. 2437–2449, 2009.

[34] F. W. Mauldin, Jr., D. Lin, and J. A. Hossack, "The singular value filter: A general filter design strategy for PCA-based signal separation in medical ultrasound imaging," *IEEE Trans Med Imaging*, vol. 30, no. 11, pp. 1951–1964, 2011.

[35] B. Byram, K. Dei, J. Tierney, and D. Dumont, "A model and regularization scheme for ultrasonic beamforming clutter reduction," *IEEE Trans Ultrason Ferroelect Freq Contr*, vol. 62, no. 11, pp. 1913–1927, 2015.

[36] J. Shin and L. Huang, "Spatial prediction filtering of acoustic clutter and random noise in medical ultrasound imaging," *IEEE Trans Med Imaging*, vol. 36, no. 2, pp. 3396–406, 2017.

[37] R. Mallart and M. Fink, "Adaptive focusing in scattering media through sound-speed inhomogeneities: The van Cittert Zernike approach and focusing criterion," *J Acoust Soc Am*, vol. 96, no. 6, pp. 3721–3732, 1994.

[38] K. W. Hollman, K. W. Rigby, and M. O'Donnell, "Coherence factor of speckle from a multi-row probe," in *Proc IEEE Ultrason Symp*, vol. 2, 1999, pp. 1257–1260.

[39] D.-L. Liu and R. C. Waag, "Correction of ultrasonic wavefront distortion using backpropagation and a reference waveform method for time-shift compensation," *J Acoust Soc Am*, vol. 96, no. 2, pp. 649–660, 1994.

[40] P.-C. Li and M.-L. Li, "Adaptive imaging using the generalized coherence factor," *IEEE Trans Ultrason Ferroelect Freq Contr*, vol. 50, no. 2, pp. 128–141, 2003.

[41] J. Camacho, M. Parrilla, and C. Fritsch, "Phase coherence imaging," *IEEE Trans Ultrason Ferroelect Freq Contr*, vol. 56, no. 5, pp. 958–974, 2009.

[42] G. F. Pinton, J. J. Dahl, and G. E. Trahey, "Impact of clutter levels on spatial covariance: Implications for imaging," in *Proc 2010 IEEE International Ultrason Symp*, 2010, pp. 2171–2174.

[43] G. F. Pinton, G. E. Trahey, and J. J. Dahl, "Spatial coherence in human tissue: Implications for imaging and measurement," *IEEE Trans Ultrason Ferroelect Freq Contr*, vol. 61, no. 12, pp. 1976–1987, 2014.

[44] M. Lediju, G. E. Trahey, B. C. Byram, and J. J. Dahl, "Short-lag spatial coherence of backscattered echoes: Imaging characteristics," *IEEE Trans Ultrason Ferroelect Freq Contr*, vol. 58, no. 7, pp. 1377–1388, 2011.

[45] R. Mallart and M. Fink, "The van Cittert-Zernike theorem in pulse echo measurements," *J Acoust Soc Am*, vol. 90, no. 5, pp. 2718–2727, 1991.
[46] W. F. Walker and G. E. Trahey, "Speckle coherence and implications for adaptive imaging," *J Acoust Soc Am*, vol. 101, no. 4, pp. 1847–1858, 1997.
[47] J. C. Lacefield and R. C. Waag, "Spatial coherence analysis applied to aberration correction using a two-dimensional array system," *J Acoust Soc Am*, vol. 112, no. 6, pp. 2558–2566, 2002.
[48] R. J. Fedewa, K. D. Wallace, M. R. Holland, J. R. Jago, G. C. Ng, M. R. Rielly, B. S. Robinson, and J. G. Miller, "Spatial coherence of the nonlinearly generated second harmonic portion of backscatter for a clinical imaging system," *IEEE Trans Ultrason Ferroelect Freq Contr*, vol. 50, no. 8, pp. 1010–1022, 2003.
[49] ——, "Spatial coherence of backscatter for the nonlinearly produced second harmonic for specific transmit apodizations," *IEEE Trans Ultrason Ferroelect Freq Contr*, vol. 51, no. 5, pp. 576–588, 2004.
[50] J. J. Dahl, D. Hyun, M. Lediju, and G. E. Trahey, "Lesion detectability in diagnostic ultrasound with short-lag spatial coherence imaging," *Ultrason Imaging*, vol. 33, no. 2, pp. 119–133, 2011.
[51] M. A. L. Bell, J. J. Dahl, and G. E. Trahey, "Resolution and brightness characteristics of short-lag spatial coherence (SLSC) images," *IEEE Trans Ultrason Ferroelect Freq Contr*, vol. 62, no. 7, pp. 1265–1276, 2015.
[52] N. Bottenus and G. E. Trahey, "Equivalence of time and aperture domain additive noise in ultrasound coherence," *J Acoust Soc Am*, vol. 137, no. 1, pp. 132–138, 2015.
[53] N. Bottenus, B. C. Byram, J. J. Dahl, and G. E. Trahey, "Synthetic aperture focusing for short-lag spatial coherence imaging," *IEEE Trans Ultrason Ferroelect Freq Contr*, vol. 60, no. 9, pp. 1816–1826, 2013.
[54] D. Hyun, A. L. C. Crowley, and J. J. Dahl, "Efficient strategies for estimating the spatial coherence of backscatter," *IEEE Trans Ultrason Ferroelect Freq Contr*, vol. 64, no. 3, pp. 500–513, 2017.
[55] J. W. Goodman, *Statistical Optics*. New York, New York: John Wiley & Sons, Inc., 1985.
[56] D. Hyun, G. E. Trahey, M. Jakovljevic, and J. J. Dahl, "Short-lag spatial coherence imaging on matrix arrays, part I: Beamforming methods and simulation studies," *IEEE Trans Ultrason Ferroelect Freq Contr*, vol. 61, no. 7, pp. 1101–1112, 2014.
[57] N. Bottenus and K. F. Ust uner, "Acoustic reciprocity of spatial coherence in ultrasound imaging," *IEEE Trans Ultrason Ferroelect Freq Contr*, vol. 62, no. 5, pp. 852–861, 2015.
[58] Y. L. Li and J. J. Dahl, "Angular coherence in ultrasound imaging: Theory and applications," *J Acoust Soc Am*, vol. 141, no. 3, pp. 1582–1594, 2017.
[59] M. Jakovljevic, G. E. Trahey, R. C. Nelson, and J. J. Dahl, "In vivo application of short lag spatial coherence imaging in human livers," *Ultrasound Med Biol*, vol. 39, no. 3, pp. 534–542, 2013.
[60] M. Jakovljevic, B. C. Byram, D. Hyun, J. J. Dahl, and G. E. Trahey, "Short-lag spatial coherence imaging on matrix arrays, part II: Phantom and in vivo experiments," *IEEE Trans Ultrason Ferroelect Freq Contr*, vol. 61, no. 7, pp. 1113–1122, 2014.
[61] J. J. Dahl, M. Jakovljevic, G. F. Pinton, and G. E. Trahey, "Harmonic spatial coherence imaging: An ultrasonic imaging method based on backscatter coherence," *IEEE Trans Ultrason Ferroelect Freq Contr*, vol. 59, no. 4, pp. 648–659, 2012.
[62] M. A. L. Bell, R. Goswami, J. A. Kisslo, J. J. Dahl, and G. E. Trahey, "Short-lag spatial coherence imaging of cardiac ultrasound data: initial clinical results," *Ultrasound Med Biol*, vol. 39, no. 10, pp. 1861–1874, 2013.
[63] D. Hyun, G. E. Trahey, and J. J. Dahl, "Real-time high-framerate *in vivo* cardiac slsc imaging with a GPU-based beamformer," in *Proc 2015 IEEE International Ultrason Symp*, 2015, dOI: 10.1109/ULTSYM.2015.0077.
[64] V. Kakkad, J. Dahl, S. Ellestad, and G. Trahey, "In vivo application of short-lag spatial coherence and harmonic spatial coherence imaging in fetal ultrasound," *Ultrason Imaging*, vol. 37, no. 2, pp. 101–116, 2015.
[65] Y. Li and J. J. Dahl, "Coherent flow power doppler (CFPD): Flow detection using spatial coherence beamforming," *IEEE Trans Ultrason Ferroelect Freq Contr*, vol. 62, no. 6, pp. 1022–1035, 2015.
[66] Y. L. Li, D. Hyun, L. Abou-Elkacem, J. K. Willmann, and J. J. Dahl, "Visualization of small-diameter vessels by reduction of incoherent reverberation with coherent flow power doppler," *IEEE Trans Ultrason Ferroelect Freq Contr*, vol. 63, no. 11, pp. 1878–1889, 2016.
[67] N. Ghandi, S. Kim, P. Kazanzides, and M. A. L. Bell, "Accuracy of a novel photoacoustic-based approach to surgical guidance performed with and without a tele-operated da vinci robot," in *Proc SPIE Photonics West*, 2016.
[68] M. A. L. Bell, A. K. Ostrowski, K. Li, P. Kazanzides, and E. M. Boctor, "Localization of transcranial targets for photoacoustic-guided endonasal surgeries," *Photoacoustics*, vol. 3, pp. 78–87, 2015.
[69] M. A. L. Bell, N. P. Kuo, D. Y. Song, J. U. Kang, and E. M. Boctor, "In vivo visualization of prostate brachytherapy seeds with photoacoustic imaging," *J Biomed Opt*, vol. 19, no. 12, p. 126011, 2014.
[70] M. A. L. Bell, N. Kuo, D. Y. Song, and E. M. Boctor, "Short-lag spatial coherence beamforming of photoacoustic images for enhanced visualization of prostate brachytherapy seeds," *Biomed Opt Express*, vol. 4, no. 10, pp. 1964–1977, 2013.
[71] M. A. L. Bell, X. Guo, D. Y. Song, and E. M. Boctor, "Transurethral light delivery for prostate photoacoustic imaging," *J Biomed Opt*, vol. 20, no. 3, p. 036002, 2015.